

Numerical simulation of a spherical dynamo excited by a flow of von Karman type

PAUL H. ROBERTS[†], GARY A. GLATZMAIER[‡] and THOMAS L. CLUNE[§][†]*Institute of Geophysics & Planetary Physics, University of California, Los Angeles, CA 90095, USA*[‡]*Earth & Planetary Sciences Department, University of California, Santa Cruz, CA 95064, USA*[§]*NASA Goddard Space Flight Center, Greenbelt, MD 20771, USA**(Received 00 Month 200x; in final form 00 Month 200x)*

In a celebrated recent experiment, Monchaux *et al.* (2007) created a self-excited dynamo in a cylindrical container of liquid sodium by a turbulent flow created by counter-rotating impellers at the plane ends of the container. A strange feature of the experiment was its failure to generate magnetic field when the impellers were made of stainless steel; success required the impellers to be made of soft iron. The results reported here were generated by numerical simulations of an idealization of the experiment. The container is a sphere and the impellers are replaced by a differential zonal motion of its surface, the northern and southern hemispheres turning about the symmetry axis in opposite senses, the whole system being contained in a thin shell with which it is in perfect electrical contact. This shell has generally a finite electrical conductance and a magnetic permeability that can greatly exceed that of the fluid. The electrodynamic effect of the shell is represented by a thin wall boundary condition, similar but not identical to that used in MHD duct flow theory. Eleven cases were considered in four of which the surface shell is an electrical insulator; in the others it is made of a conducting material which, like soft iron, might have a large permeability. In eight cases, a seed field decays away but in three it is amplified and becomes a turbulent self-excited dynamo. Through four cases of the same surface motion and shell permeability, it is inferred that an increase in the shell conductance assists regeneration of magnetic field. It is also shown that enhancing the shell permeability assists field creation.

Keywords: homogeneous dynamos, VKS experiment, thin wall approximation

1 Introduction

Considerable excitement was created in 2007 amongst those studying homogeneous dynamos by the news that a comparatively simple laboratory experiment had maintained a magnetic field (Monchaux *et al.* 2007). The excitement was not because of the field creation itself, remarkable though that was. Homogeneous dynamos in the laboratory had already been constructed by Lowes and Wilkinson (1968), Gailitis *et al.* (2001) and Stieglitz and Müller (2001). But these dynamos were in highly constrained geometries, the Lowes and Wilkinson model, that had solid moving parts, being the most highly constrained of all. In contrast, the fluid flow of Monchaux *et al.* (2007), described in the abstract above, was unconstrained other than by the container and impellers. And the moving fluid in their experiment was turbulent, as is surely the fluid in every naturally occurring dynamo. The excitement and fame of their experiment was surely justified. And yet there was a curious fact; magnetic field was sustained only if the impellers stirring the liquid sodium in their experiment were made of soft iron, which has a high magnetic permeability, rather than stainless steel, which does not. This deviation from the desired homogeneity of the experiment was unfortunate but unavoidable, given the available power supply. It seemed very likely that the inhomogeneity was not an essential ingredient of their dynamo and that an increase in the rotation speed of stainless steel impellers, were it possible, would have maintained the magnetic field equally well.

2 The model

Our simulations of more than a decade ago (Glatzmaier and Roberts 1995, 1996) initiated what is by now a thriving industry amongst theoreticians that has already created innumerable self-excited, three-

dimensional, magnetohydrodynamic dynamos, i.e., dynamos that satisfy not only the dictates of electromagnetism but also obey the fluid dynamic equations. The majority of these studies try to simulate the geodynamo, for which the flow is driven by thermal buoyancy and/or compositional buoyancy. They therefore have to add the heat conduction equation and/or the equation that governs composition to the pre-Maxwell and Navier-Stokes equations in the fluid volume. This is unnecessary when simulating the VKS experiment which is driven from the boundaries purely mechanically. In this respect, the task is simpler than solving the geodynamo equations. Assuming the fluid is incompressible, we must solve

$$\nabla \cdot \mathbf{V} = 0, \quad \nabla \cdot \mathbf{B} = 0, \quad (1a,b)$$

$$\partial_t \mathbf{V} + \mathbf{V} \cdot \nabla \mathbf{V} = -\nabla P / \rho + \mathbf{J} \times \mathbf{B} / \rho + \nu \nabla^2 \mathbf{V}, \quad (1c)$$

$$\partial_t \mathbf{B} = \nabla \times (\mathbf{V} \times \mathbf{B}) + \eta \nabla^2 \mathbf{B}, \quad (1d)$$

where \mathbf{V} is fluid velocity, \mathbf{B} is magnetic field, $\mathbf{J} = \mu^{-1} \nabla \times \mathbf{B}$ is electric current density, P is the pressure perturbation, ρ is density, ν is kinematic viscosity, $\eta = 1/\mu\sigma$ is magnetic diffusivity, μ is magnetic permeability, σ is electrical conductivity, and the time derivative is $\partial_t = \partial/\partial t$; SI units are used, and ρ , ν , η , μ and σ are constants. Coriolis forces are neglected since this system is solved in the laboratory frame of reference..

Any but spherical or planar boundaries are hard to deal with in dynamo simulations. Even spheroidal containers raise troublesome obstacles, as the papers of Schmitt and Jault (2004) and Wu and Roberts (2009) show. The cylindrical configuration of the VKS experiment is even more difficult to simulate (except in one particular limit mentioned below). Fortunately, the particular issue raised in Section 1 about the VKS experiment is unconnected to its cylindrical geometry. We therefore make the simplest assumption, supposing that the fluid is confined to a deep spherical shell V with outer boundary S_o and inner boundary S_i of radii r_o and r_i respectively. The inner boundary is included so that we can make use of a tested computer program that we have available. The region $r < r_i$ is taken to be a solid electrical insulator. We adopt the usual toroidal/poloidal representation of flow and field:

$$\mathbf{V} = \nabla \times (Z\hat{\mathbf{r}}) + \nabla \times [\nabla \times (W\hat{\mathbf{r}})], \quad \mathbf{B} = \nabla \times (J\hat{\mathbf{r}}) + \nabla \times [\nabla \times (B\hat{\mathbf{r}})], \quad (2a,b)$$

where $\hat{\mathbf{r}}$ is the unit radial vector. The scalars Z , W , J and B are functions of t and the spherical polar coordinates (r, θ, ϕ) . They are expanded in spherical harmonics, e.g.,

$$Z(r, \theta, \phi, t) = \sum_{\ell, m} Z_{\ell}^m(r, t) Y_{\ell}^m(\theta, \phi), \quad (2c)$$

where $Y_{\ell}^m(\theta, \phi)$ are fully normalized spherical harmonics. We have chosen a rhomboidal truncation of spherical harmonics such that $0 \leq m \leq M$ and $m \leq \ell \leq M + m + 1$, where M was either 47 or 255. The complex spherical harmonic coefficients, e.g., $Z_{\ell}^m(r, t)$, are further expanded in Chebyshev polynomials up to degree 80 or 240. Further details about this and the spectral transform method used to integrate (1) can be found in Glatzmaier (1984) and Glatzmaier and Roberts (1996); the parallel programming method is described in Glatzmaier and Clune (2000).

We assume that S_i is impermeable and that the tangential stresses across it can be ignored. Solutions to (1) must then satisfy

$$\partial_r Z_{\ell}^m(r_i, t) - \frac{2}{r_i} Z_{\ell}^m(r_i, t) = 0, \quad W_{\ell}^m(r_i, t) = 0, \quad \partial_r^2 W_{\ell}^m(r_i, t) - \frac{2}{r_i} \partial_r W_{\ell}^m(r_i, t) = 0, \quad (3a,b,c)$$

where $\partial_r = \partial/\partial r$. The sphere S_i is supposed filled by an electrical insulator, so that

$$J_\ell^m(r_i, t) = 0, \quad \partial_r B_\ell^m(r_i, t) - \frac{(\ell + 1)}{r_i} B_\ell^m(r_i, t) = 0, \quad (3d,e)$$

assuming the inner core has the same magnetic permeability as the fluid.

The outer boundary is impermeable and non-slip but has a prescribed zonal velocity that depends on colatitude θ . In the general case, this is given by the zero- m terms of (2c), with $Z_\ell^0(r_o, t)$ set to assigned constant values, v_ℓ , say. We simplified by retaining only the v_1 and v_2 terms, rewriting (2c) on S_o as

$$V_\phi(r_o, \theta, \phi, t) = U_1 \sin \theta + U_2 \sin \theta \cos \theta. \quad (4a)$$

The constant U_2 quantifies a shear between the northern and southern hemispheres of the container, and is intended to mimic the differential motion of the impellers in the VKS experiment; the constant U_1 imposes an added ‘‘solid body’’ rotation on the system relative to the laboratory frame of reference. The outer boundary conditions on \mathbf{V} are therefore

$$W_\ell^m(r_o, t) = 0, \quad \partial_r W_\ell^m(r_o, t) = 0, \quad \text{for all } \ell, m, \quad (4b,c)$$

together with

$$Z_1^0(r_o, t) = \left(\frac{4\pi}{3}\right)^{\frac{1}{2}} r_o U_1, \quad Z_2^0(r_o, t) = \frac{1}{3} \left(\frac{4\pi}{5}\right)^{\frac{1}{2}} r_o U_2, \quad \text{all other } Z_\ell^m(r_o, t) = 0. \quad (4d,e,f)$$

We derive boundary conditions on \mathbf{B} on S_o in the next section.

Our model has some similarities to the models of Kaiser and Tilgner (1999), Gissinger *et al.* (2008b) and Ravelet *et al.* (2005). In those models, however, the flow is either prescribed or is driven by a prescribed volumetric body force. Our model has a closer connection to one of four considered by Spence *et al.* (2009), a paper that had not been published when we made our presentation at the Nice meeting. Their fourth main case has nonzero v_2, v_4, v_6 and v_8 , the other v_ℓ being zero. The resulting $V_\phi(r_o)$ is shown in their figure 4. It vanishes at the poles, is antisymmetric with respect to the equatorial plane and has a single extremum at mid-latitudes in each hemisphere at $\theta \approx \pm 60^\circ$; ours shares these properties when $U_1 = 0$, but has its extrema at $\theta = \pm 45^\circ$. The main difference between their model and ours is the absence in their model of the thin conducting shell of higher permeability that we suppose may exist and be in electrical contact with the fluid on S_o ; see below. A significant departure from the VKS experiment is the absence of blades on the impellers, so that the zonal motion of S_o is transmitted to the fluid only through the boundary layers that form on the surface of the fluid. We consider the case $U_1 = 0$ only in this paper.

3 Thin wall conditions

Thin wall boundary conditions are often used in simulations of laboratory experiments on the flow of liquid metals in magnetic fields. When the container walls are electrically conducting, electric currents can leak into them from the fluid and can be electrodynamically induced in them through the time dependence of \mathbf{B} in the fluid. If it is required to represent the effects of these currents in detail, the three-dimensional time-dependent magnetic field would need to be calculated within the walls and the final results would depend on parameters representing the thickness and conductivity of the walls. This additional complication can, however, be minimized if less detail is sought. The thin wall conditions are an approximation commonly used in modeling duct flow of liquid metals; see, for example, sections 3.2.2 of Müller and Bühler (2001). A limiting process is envisaged in which the thickness, h , of the container walls tends to zero while their electrical conductivity, σ_W , tends to infinity, in such a way that their product, the conductance of the wall, remains finite. It is then unnecessary to solve the induction equation in the wall. The conductance of the wall is represented merely by a modification to the conditions applied to \mathbf{B} at the wall. This thin-wall

approximation was employed by Glatzmaier and Roberts (1995, 1996) in their geodynamo simulations in order to recognize electrical conduction in the Earth's mantle, which is most significant at great depths.

In this section, we derive a modification of the thin wall conditions. The modification is required since we seek to study how the inclusion of ferromagnetism in the walls affects the dynamo driven at the walls. We generalize the idea of a thin wall condition by assuming that, as $h \rightarrow 0$, the magnetic permeability, μ_W , of the wall tends to infinity, in such a way that the product $h\mu_W$, remains finite. More precisely, we introduce two parameters,

$$c = \frac{h\mu_W}{r_o\mu_F} \quad \text{and} \quad c' = \frac{h\sigma_W}{r_o\sigma_F}. \quad (5a,b)$$

Here, in studying the transition to $h = 0$, we suppose the system consists of 3 regions, the conducting fluid (F), the conducting wall (W) and the external insulating atmosphere or vacuum (V). The interfaces between the regions are denoted by S_{FW} and S_{WV} and are supposed to have a common unit normal \mathbf{n} directed from F into V . The plan is to apply the usual continuity conditions on the field at these interfaces and to represent the field within the wall as a Taylor expansion in the thin-wall limit to arrive at boundary conditions on the field at the outer edge of the fluid in terms of the potential field outside the wall.

As in (4), no-slip boundary conditions are assumed on S_{FW} :

$$\mathbf{V}_F = \mathbf{V}_W, \quad \text{on} \quad S_{FW}. \quad (6)$$

The normal component, $\mathbf{n}\cdot\mathbf{B}$, of the magnetic field, \mathbf{B} , and the tangential components, $\mathbf{n}\times\mathbf{H}$, of the magnetizing force, $\mathbf{H} = \mathbf{B}/\mu$, are continuous across both wall surfaces:

$$\mathbf{n}\cdot\mathbf{B}_F = \mathbf{n}\cdot\mathbf{B}_W, \quad \mathbf{n}\times\mathbf{H}_F = \mathbf{n}\times\mathbf{H}_W, \quad \text{on} \quad S_{FW}, \quad (7a,b)$$

$$\mathbf{n}\cdot\mathbf{B}_W = \mathbf{n}\cdot\mathbf{B}_V, \quad \mathbf{n}\times\mathbf{H}_W = \mathbf{n}\times\mathbf{H}_V, \quad \text{on} \quad S_{WV}. \quad (7c,d)$$

Conditions (6) and (7a) imply that $\mathbf{n}\times(\mathbf{V}\times\mathbf{B})$ is continuous across S_{FW} , so that the condition on the electric field \mathbf{E} there, i.e.,

$$\mathbf{n}\times\mathbf{E}_F = \mathbf{n}\times\mathbf{E}_W, \quad \text{on} \quad S_{FW}, \quad (7e)$$

implies

$$\mathbf{n}\times(\mathbf{E} + \mathbf{V}\times\mathbf{B})_F = \mathbf{n}\times(\mathbf{E} + \mathbf{V}\times\mathbf{B})_W, \quad \text{on} \quad S_{FW}. \quad (7f)$$

It therefore follows from Ohm's law, $\mathbf{J} = \sigma(\mathbf{E} + \mathbf{V}\times\mathbf{B})$, that

$$(\mathbf{n}\times\mathbf{J}/\sigma)_F = (\mathbf{n}\times\mathbf{J}/\sigma)_W, \quad \text{on} \quad S_{FW}. \quad (8)$$

A condition similar to (7e) also applies on S_{WV} , namely $\mathbf{n}\times\mathbf{E}_W = \mathbf{n}\times\mathbf{E}_V$, but this does not restrict the solution for \mathbf{B}_F and will not be considered further. Only condition (7e) matters in what follows.

We now assume that h is small. More precisely, we suppose that, if L and T are typical length and time scales of the electromagnetic field outside the wall, then $h \ll L$ and $h \ll (T\eta_W)^{1/2}$, where $\eta_W = 1/\mu_W\sigma_W$ is the magnetic diffusivity of the conducting wall. The second of these conditions (and Faraday's law of induction) ensures that $(\mathbf{n}\times\mathbf{E})_W$ is nearly uniform within the wall, so that $(\mathbf{n}\times\mathbf{J}/\sigma)_W$ is nearly uniform also. Because $\sigma_W \rightarrow \infty$ in the contemplated limit, the wall may carry a net current \mathcal{J} , resulting in a finite change in $\mathbf{n}\times\mathbf{H}$ and $\mathbf{n}\times\mathbf{B}$ across the wall. Because $\mu_W \rightarrow \infty$ in the limit, there is also generally a net change in $\mathbf{n}\cdot\mathbf{H}$ and $\mathbf{n}\cdot\mathbf{B}$.

We now return to the case of a spherical S_{FW} , of radius r_o , and the representation (2b). This implies

$$\mu \mathbf{J} = -\nabla \times [(\nabla_1^2 B) \hat{\mathbf{r}}] + \nabla \times [\nabla \times (J \hat{\mathbf{r}})], \quad (9a)$$

where

$$\nabla_1^2 = \partial_r^2 - \frac{L^2}{r^2}, \quad L^2 = - \left[\frac{1}{\sin \theta} \frac{\partial}{\partial \theta} \left(\sin \theta \frac{\partial}{\partial \theta} \right) + \frac{1}{\sin^2 \theta} \frac{\partial^2}{\partial \phi^2} \right], \quad \text{and so} \quad \nabla^2 = \nabla_1^2 + \frac{2}{r} \partial_r. \quad (9b,c,d)$$

The boundary conditions (7a-d) give

$$[[B]] = 0, \quad [[\mu^{-1} \partial_r B]] = 0, \quad [[\mu^{-1} J]] = 0, \quad \text{at} \quad \zeta = 0, 1, \quad (10a,b,c)$$

where $\zeta = (r - r_o)/h$ is a scaled normal coordinate in the wall and $[[f]]$ is the jump in a function f at either boundary of the wall. Recall that here B and J are the magnetic poloidal and toroidal scalar functions, respectively, as defined in (2b), not the magnitudes of the magnetic field and electric current density. When there is a finite change in $\mathbf{n} \times \mathbf{B}$ across the wall, B_W varies rapidly in ζ and $\partial_r^2 B_W \gg L^2 B_W / r_o^2$. Condition (8) and (9a) give

$$\partial_r^2 B_W \approx \nabla_1^2 B_W = (\eta_F / \eta_W) \nabla_1^2 B_F, \quad \partial_r J_W = (\eta_F / \eta_W) \partial_r J_F, \quad \text{at} \quad \zeta = 0. \quad (10d,e)$$

Taylor expansion of J_W about $\zeta = 0$ and (10c,e) give

$$J_W(\zeta) = J_{W0} + (\partial_r J_W)_0 h \zeta + \dots = \frac{\mu_W}{\mu_F} \left[J_{F0} + \frac{h \sigma_W}{\sigma_F} (\partial_r J_F)_0 \zeta + \dots \right], \quad (11a)$$

where the suffix 0 means evaluation at $\zeta = 0$. Similarly, the Taylor expansion of B_W gives, with help from (10a,b,d),

$$B_W(\zeta) = B_{F0} + \frac{h \mu_W}{\mu_F} \left[(\partial_r B_F)_0 \zeta + \frac{h \sigma_W}{2 \sigma_F} (\nabla_1^2 B_F)_0 \zeta^2 + \dots \right], \quad (11b)$$

$$\partial_r B_W(\zeta) = \frac{\mu_W}{\mu_F} \left[(\partial_r B_F)_0 + \frac{h \sigma_W}{\sigma_F} (\nabla_1^2 B_F)_0 \zeta + \dots \right]. \quad (11c)$$

When we take the limit $h \rightarrow 0$, with the parameters (5) held fixed, the higher-order terms represented by \dots in the expansions of the last paragraph vanish. The results (11a-c) and the boundary conditions (7c,d) give

$$[[B]] = -c r_o \partial_r B - \frac{1}{2} r_o^2 c c' \nabla_1^2 B, \quad \text{on} \quad r = r_o, \quad (12a)$$

$$[[\mu^{-1} \partial_r B]] = -c' r_o \mu^{-1} \nabla_1^2 B, \quad [[\mu^{-1} J]] = -c' r_o \mu^{-1} \partial_r J, \quad \text{on} \quad r = r_o, \quad (12b,c)$$

where now $[[f]] = f - \hat{f}$. We have here deleted the suffix F on values in the fluid, and have added a hat to distinguish vacuum values. The surfaces S_{FW} and S_{WV} have collapsed into the single surface S_o .

In the vacuum \hat{V} outside the fluid

$$\nabla_1^2 \hat{B} = 0, \quad \hat{J} \equiv 0. \quad (13a,b)$$

When \widehat{B} is divided into its spherical component parts as in (2c), the condition that there are no sources of field outside S and (13a) give

$$\widehat{B}_\ell^m \propto r^{-\ell}, \quad \text{which implies} \quad \partial_r \widehat{B}_\ell^m = -\frac{\ell}{r} \widehat{B}_\ell^m. \quad (13c,d)$$

On using (13d) to eliminate \widehat{B}_ℓ^m from the harmonic components of (12a,b) and applying (13b), we obtain

$$\frac{\widehat{\mu}}{\mu} \partial_r B_\ell^m + \frac{\ell}{r_o} B_\ell^m = -c \ell \partial_r B_\ell^m - c' r_o \left(\frac{\widehat{\mu}}{\mu} + \frac{c \ell}{2} \right) \left[\partial_r^2 B_\ell^m - \frac{\ell(\ell+1)}{r_o^2} B_\ell^m \right], \quad \text{on} \quad r = r_o, \quad (14a)$$

$$J_\ell^m = -c' r_o \partial_r J_\ell^m, \quad \text{on} \quad r = r_o. \quad (14b)$$

Equations (14a,b) are our generalization of the thin wall conditions. They reduce for $c = 0$ to the thin wall conditions used by Glatzmaier and Roberts (1995) to include the effects of the conducting material in deep Earth's mantle. If instead we set $c' = 0$ but take $c \neq 0$, boundary conditions (14a,b) simplify to

$$\frac{\widehat{\mu}}{\mu} \partial_r B_\ell^m + \frac{\ell}{r_o} B_\ell^m = -\frac{c \ell}{r_o} \partial_r B_\ell^m, \quad J_\ell^m = 0, \quad \text{on} \quad r = r_o. \quad (15a,b)$$

In the limit $c \rightarrow \infty$, (15a,b) imply $\mathbf{n} \times \mathbf{B} = \mathbf{0}$ on S . This boundary condition is a very convenient one, and was adopted by Kageyama *et al.* (1995) in their early dynamo simulations. It is also a condition that is easily applied to non-spherical containers, such as that of the VKS experiment; see Gissinger *et al.* (2008a). This simplification is not available when c is finite. For the models of Spence *et al.* (2009), $c = c' = 0$.

The effect of the walls is easily seen by studying the *decay modes*, i.e., by calculating the decay rate, $\lambda = z^2 \eta / r_o^2$, of fields when \mathbf{u} is zero. The simplest case to consider is when the entire interior of S_o is conducting. Then, $B_\ell, J_\ell \propto r j_\ell(zr/r_o)$, where $j_\ell(z)$ is the spherical Bessel function of the first kind. For a dipolar field ($\ell = 1$) and $\mu = \mu_0$, (14a,b) reduce to

$$\frac{\tan z}{z} = \frac{2c + c'(2+c)z^2}{2c + c'(2+c)z^2 - 2(1+c)z^2}, \quad \frac{\tan z}{z} = \frac{c' - 1}{c' - 1 - c'z^2}. \quad (15c,d)$$

These transcendental equations have an infinity of positive roots, the smallest of which gives the mode that decays most slowly. For (15c), this is given for large c' by

$$z^2 \sim 2(3 + 2c)/(2 + c)c', \quad c' \rightarrow \infty. \quad (15e)$$

The corresponding λ tends to zero because the toroidal currents in the boundary shell decide the decay rate of the poloidal field in this limit. The smallest z for other c and c' are given in the upper part of table 1. For $c' \approx 0.461578$, the poloidal λ is independent of c and $z^2 = 4.332958$ (for which $\tan z = 2z/(2 - z^2)$ and $c' = 2/z^2$). For smaller (larger) c' , λ is a decreasing (increasing) function of c . This suggests that increasing the μ of the impellers helps regeneration only if their σ is not too large. (This conjecture is not strongly supported by cases 6 and 10 in section 4.)

A case more relevant to section 4 is that in which $r < r_i$ is filled by insulator and in which therefore $B_\ell, J_\ell \propto r[j_\ell(zr/r_o) - C y_\ell(zr/r_o)]$, where $y_\ell(z)$ is the spherical Bessel function of the second kind and C is a constant which is determined through the boundary conditions (3d,e). Results for $r_i = 0.2r_o$ are shown in the lower part of table 1.

Table 1: Decay rates $z^2 = \lambda r_o^2 / \eta$ of dipolar decay modes							
$r_i = 0$							
c	Poloidal modes			c'	Poloidal modes		Toroidal mode
	c' = 0 z^2	c' = 0.3 z^2	c' = 2 z^2		c = 0 z^2	c = 10 z^2	
0	9.8696	5.5327	1.3585	0	9.8696	7.7721	20.191
0.1	9.6852	5.5063	1.3739	0.1	8.0446	6.7407	16.826
0.3	9.3914	5.4631	1.4002	0.3	5.5327	5.1951	13.254
0.6	9.0750	5.4148	1.4315	0.6	3.6370	3.7790	11.078
1	8.7891	5.3697	1.4629	1	2.4674	2.7393	9.870
2	8.3903	5.3040	1.5126	2	1.3585	1.6074	8.789
4	8.0560	5.2463	1.5607	4	0.7136	0.8759	8.183
10	7.7721	5.1951	1.6074	10	0.2941	0.3696	7.796
20	7.6567	5.1737	1.6281	20	0.1485	0.1882	7.663
∞	7.5279	5.1495	1.6526	$\rightarrow \infty$	$3/c'$	$23/6c'$	7.528
$r_i = 0.2r_o$							
c	Poloidal modes			c'	Poloidal modes		Toroidal mode
	c' = 0 z^2	c' = 0.3 z^2	c' = 2 z^2		c = 0 z^2	c = 10 z^2	
0	9.9102	5.5346	1.3586	0	9.8820	7.7793	21.962
0.1	9.7227	5.5082	1.3739	0.1	8.0508	6.7453	17.993
0.3	9.4244	5.4650	1.4002	0.3	5.5346	5.1973	13.976
0.6	9.1037	5.4168	1.4316	0.6	3.6376	3.7799	11.613
1	8.8145	5.3717	1.4630	1	2.4676	2.7397	10.324
2	8.4117	5.3061	1.5127	2	1.3586	1.6075	9.181
4	8.0747	5.2484	1.5608	4	0.7136	0.8760	8.544
10	7.7886	5.1973	1.6075	10	0.2941	0.3696	8.138
20	7.6725	5.1759	1.6282	20	0.1485	0.1882	7.999

4 Preliminary results

In table 2, we summarize preliminary results from 11 cases that survey sensitivity to the prescribed surface shear flow amplitude, U_2 , introduced in (4a), and to the parameters c and c' defined in (5). The following values for the fluid were assumed for all cases:

$$r_i = 0.1\text{m}, \quad r_o = 0.5\text{m}, \quad \eta = 0.083\text{m}^2\text{s}^{-1}, \quad \nu = 0.01\eta, \quad \rho = 930\text{kg m}^{-3}. \quad (16)$$

Apart from the viscosity, these are realistic values for a liquid sodium experiment roughly the size of the VKS experiment (Monchaux *et al.* 2007). The molecular kinematic viscosity of liquid sodium is about 5×10^{-6} times smaller than its magnetic diffusivity, η . Here, because of computational limitations, the magnetic Prandtl number $Pm = \nu/\eta$ was set to only 0.01, so that ν should be regarded as a crude representation of a turbulent viscosity. The magnetic permeability of the fluid, μ , and that of the external atmosphere, $\hat{\mu}$, were set to the free-space value, $\mu_0 = 4\pi \times 10^{-7}\text{H m}^{-1}$. For the parameters (16), our typical computational timestep was 10^{-5}s , which may be compared with the magnetic diffusion time, $\tau \approx 3.01z^{-2}$, defined by the dipole component of \mathbf{B} , which according to section 3 is between $\frac{1}{4}\text{s}$ and $2\frac{1}{4}\text{s}$ for the cases considered in table 2. Except for case 9 which was started from case 10, the simulations were initiated from a state of rest, in a uniform seed field of 1G parallel to the ‘‘polar’’ axis $\theta = 0$.

Table 2 contains a brief summary of our results. We chose several combinations of the parameters c and c' . Cases with both parameters set to zero represent insulating walls or the limit of very thin stainless steel

walls. Cases with $c = 0$ but c' finite represent walls with a conductance, $h\sigma_W$, comparable to $r_o\sigma$ for the fluid. The opposite specification, $c' = 0$ and c finite, represents walls with $h\mu_W$ comparable to or larger than $r_o\mu_0$ for the fluid. Case 11 is constrained to have the field normal to the outer boundary. For cases 8–10 both parameters are finite.

Table 2 also lists the prescribed values of the shear parameter, U_2 . Three different values of this parameter were chosen, which differ by factors of 5. The solid body rotation parameter, U_1 , was set to zero for all cases considered here. The magnetic Reynolds number, which measures how well magnetic induction counters magnetic diffusion, is defined as

$$Rm = \frac{U_2 r_o}{2\eta}. \quad (17)$$

The factor of 2 is included because the peak driving velocity is $U_2/2$ according to (4a). The three values of U_2 in table 2 correspond to Rm of 10, 48 and 240 and hydrodynamic Reynolds numbers Re of 1000, 4800 and 24000. The Rm values somewhat over-estimate inductive effects because peak velocities occur only near the outer boundary. Moreover the zonal motion created in V by the imposed motion of S_o cannot, by the toroidal velocity theorem, support a dynamo unaided. Regeneration requires poloidal flow, such as that provided by Ekman pumping from S_o . Also, Cowling's theorem requires asymmetry such as that provided by an instability of the basic zonal flow.

The duration of the integration for each case is also listed in table 2 in the column labeled 'time'. Ten seconds typically requires a million computational time steps. The final column of the table gives the approximate peak field intensities generated by the fluid motion; $|\mathbf{B}| \rightarrow 0$ indicates that the field decays, either monotonically or after an initial brief period of growth. Only cases 6, 9 and 10 produced fields that seem to be permanent, albeit with time dependent amplitudes. For those that fail as dynamos, the larger the value of U_2 the more slowly the field decays. This may be seen by comparing the two τ columns of table 2. The first of these, labeled $\tau(U_2 \neq 0)$, was derived from the evolution of the field energy in the conducting region V :

$$M(t) = \frac{1}{2\mu_0} \int_V B^2 dV. \quad (18)$$

After the transients associated with the start of the integration had subsided, $M(t)$ decayed approximately exponentially, though with some superimposed variability, especially for the conducting-wall cases with larger U_2 for which the turbulent fluctuations have greater amplitude. The determination of the decay rate [2τ for $M(t)$] was therefore subject to an uncertainty, indicated by the \pm magnitudes in the entries. It may be seen however that the mean value, in every case but case 5, equals or exceeds the corresponding value in the next column, labeled $\tau(U_2 = 0)$, which gives the τ obtained using the programs that generated table 1. In the extreme cases 6, 9 and 10, the decay time $\tau(U_2 \neq 0)$ is meaningless, being essentially infinite! Only the values of $M(t)$ in a short period immediately before the integration was terminated were used to evaluate $\tau(U_2 \neq 0)$. If that period was one in which the superimposed oscillation of $M(t)$ is in a decreasing phase, the corresponding mean value of $\tau(U_2 \neq 0)$ will be too short. This may explain the anomalously small value of $\tau(U_2 \neq 0)$ in case 5. The field in case 11 initially grew from a peak value of 1.0 G to 1.5 G, but then decayed to about 2×10^{-3} G by $t = 3.6$ s. It is mysterious that all our $c' = 0$ cases, even case 11, fail as dynamos., but model 4 of Spence *et al.* (2009), for which $c = c' = 0$, regenerated field for $Rm > Rm_{crit} = 274$ and $Pm = 1$. They observed however that it did not self-excite for $Pm = 0.5$. They concentrated on the case $Rm = 2000$ and $Pm = 1$.

Case 6 is unquestionably a dynamo. Its axial dipole dominates its equatorial dipole, indicating that its Rm greatly exceeds the marginal value, for which the magnetic field would have been entirely asymmetric, according to Cowling's theorem. The asymmetric secondary flow resulting from the instability of the prescribed axisymmetric forcing (4a) on S_o evidently has an important inductive effect. The field intensity is markedly time-dependent.

The importance of conductance in the boundary was first pointed out by Bullard and Gubbins (1977); see also Garaud and Guervilly (2008) and Soward and Dormy (2009). It is illustrated here by the effect

of increasing c' for the four cases 7–10, while retaining the same values of U_2 ($= 80\text{m s}^{-1}$) and c ($=10$); cases 7 and 8 fail as dynamos, while cases 9 and 10 succeed. Though small, the value of c' for case 8 suffices to lengthen noticeably the decay time of field, as compared with case 7; compare columns 6 and 7 of table 2. Cases 6 and 10, share the same values of U_2 and c' ($=2$), the larger c of case 10 resulting in a greater field amplitude $|\mathbf{B}|$, indicating that soft iron in the impelling wall enhances dynamo action. This represents a limited refutation of the conjecture made in section 3 that the wall conductivity (c') needs to be sufficiently small for a large wall magnetic permeability (c) to assist field regeneration.

Table 2: Summary of cases integrated							
Case	c	c'	U_2 m s ⁻¹	Time s	τ ($U_2 \neq 0$) s	τ ($U_2 = 0$) s	Maximum Field ($ \mathbf{B} _{\text{max}}$) Gauss
1	0	0	3.2	9.1	0.31±0.001	0.30	$ \mathbf{B} \rightarrow 0$
2	0	2	3.2	15.0	2.24±0.01	2.22	$ \mathbf{B} \rightarrow 0$
3	0	0	16.	3.0	0.31±0.001	0.30	$ \mathbf{B} \rightarrow 0$
4	0	2	16.	41.0	2.99±0.25	2.22	$ \mathbf{B} \rightarrow 0$
5	0	0	80.	4.3	0.28±0.002	0.30	$ \mathbf{B} \rightarrow 0$
6	0	2	80.	15.8	SSS*	2.22	$ \mathbf{B} \sim 2600$
7	10	0	80.	3.7	0.42±0.02	0.39	$ \mathbf{B} \rightarrow 0$
8	10	0.02	80.	8.8	0.50±0.03	0.39	$ \mathbf{B} \rightarrow 0$
9	10	0.2	80.	18.9	SSS†	0.51	$ \mathbf{B} \sim 1400$
10	10	2	80.	15.5	SSS‡	1.87	$ \mathbf{B} \sim 3500$
11	∞	0	80.	3.6	0.44±0.03	0.39	$ \mathbf{B} \rightarrow 0$

* † ‡ Statistically Steady Solutions (SSS). Mean magnetic energies:
 $\bar{M} \approx * 3 \times 10^3\text{J}$, † $9 \times 10^2\text{J}$, ‡ $4 \times 10^3\text{J}$.

A snapshot of the fluid flow for case 9 is shown in figure 1. The angular velocity of the fluid within the outer boundary layer is eastward in the northern hemisphere (solid contours) and westward in the southern hemisphere (broken contours) but the bulk of the interior has very little angular velocity as the top left-hand image shows. This indicates that a significant ω -effect exists within the shallow outer boundary layer that tends to wind up axisymmetric poloidal field into eastward directed toroidal field in both hemispheres, as seen in figure 2. This is a significant ingredient in the process that creates the strong axisymmetric field characterizing dynamos of VKS type. The two lower images show that the meridional circulation of the fluid is downward, towards S_i , in the equatorial region and upward, towards S_o , at high latitudes, as expected from Ekman pumping. The magnetic field illustrated in figure 2 is a snapshot at the same instant as that displayed in figure 1. The eastward-directed toroidal field component peaks on the surface at mid-latitude in each hemisphere but, because of the large magnetic diffusion relative to viscous diffusion, is not so confined to a shallow boundary layer as is the zonal flow. Based on the curl of this axisymmetric eastward-directed magnetic field, the axisymmetric part of the current density below S_o is directed northward in both hemispheres. On S_o in the northern hemisphere, the current is also directed outward into the conducting wall at high latitude and inward from the wall at low latitude; the opposite is true in the southern hemisphere. Therefore, there are meridional electric circuits between the fluid and the wall in both hemispheres when c' is non-zero. The resulting magnetic torque on fluid at S_o , especially at mid-latitude, helps to maintain the zonal boundary-layer flows in both hemispheres. The electric current in the boundary layers is also partially ϕ -directed, giving rise to the kinks in the poloidal field lines at S_o seen in the lower left panel of figure 2. The thickness of the boundary layers is of order $Rm^{-1/2}r_o$.

In cases 6 and 10, the total integrated kinetic energy of the fluid is 2–3 times greater than the magnetic energy $M(t)$, but in case 9 it is about 10 times greater. About 95% of the magnetic energy is in the axisymmetric part of the field, of which about 95% is toroidal field within the container. The kinetic energy density peaks in a shallow boundary layer, dropping off by about two orders of magnitude with depth. The magnetic energy density peaks on the outer boundary (S_o) but, on average, drops off by only about one order of magnitude with depth. The main contributions to both the kinetic and magnetic

energies are their longitudinal (zonal) components. The structures of the flows and fields in the bulk of the fluid for the other cases are quite similar to those of case 9, but their amplitudes and time dependencies are different. The evolution of $M(t)$ is shown for cases 6, 9 and 10 in the three panels of figure 3. These demonstrate convincingly that these cases maintain field and, particularly for the more strongly driven cases 9 and 10, that the dynamos are turbulent. (Note: case 9 was started from case 10 at roughly 6 seconds, which is why M for that case drops at that time.) The $M(t)$ for case 10 resembles that for case 4 of Spence *et al.* (2009) for $Rm = 2000$ and $Pm = 1$; see their figure 6. Rough mean values \bar{M} of $M(t)$ after reaching statistical equilibrium are given beneath table 2.

5 Conclusions

We have derived in this paper a generalization of the thin wall boundary conditions that are frequently used in describing laboratory flows of liquid metal in the presence of magnetic fields. The current flow into the bounding walls is computed by supposing the walls are thin but have finite conductance. Our generalization allows for the possibility that the walls are made of a material of high magnetic permeability, such as soft iron, and that their integrated permeability is finite. The importance of wall permeability and wall conductance is quantified by parameters c and c' respectively defined in (5).

We have used the thin wall conditions to simplify the study of a simple spherical dynamo model that has features in common with the VKS experiment. It has allowed us to explore some of the differences between flows driven by stainless steel or by soft iron impellers, which we have represented by differentially turning hemispheres on the outer boundary. We have found that dynamo action is aided by an outer wall having a conductance, $h\sigma_W$, comparable to that of the fluid or an integrated magnetic permeability, $h\mu_W$, larger than the fluid (as in the VKS experiment). An unexpected result was that the latter situation alone does not appear to be sufficient in our model configuration to produce a dynamo; it also requires a higher wall conductivity or thickness. A possible reason for this could be that our thin wall magnetic boundary condition with $c' = 0$ prevents electric current flow between the fluid and the wall. Kaiser and Tilgner's (1999) study of kinematic dynamos showed that, for a given geometry and flow profile, there is an optimal conducting wall thickness for dynamo action related to the current in the wall. An expected result from our study was that increasing the amount of driving shear either slows the decay of the field or accelerates its growth.

Future studies using our model might investigate the effects of

- (i) different initial magnetic field configurations, to see whether there is more than one final state for given U_2 , c and c' ;
- (ii) making $U_1 \neq 0$, so that the flows are of unequal strengths in the two hemispheres, this being a way of mimicking a similar asymmetry between the rotation of the impellers of the VKS experiment which revealed a wealth of interesting phenomena;
- (iii) a modification in the choice of the constants $A_\ell [= Z_\ell^0(r_o)]$ in (4d-f) that brings the peak of the zonal forcing, $V_\phi(r_o, \theta, \phi, t)$, closer to the poles, in order to simulate better the impellers of the VKS experiment, and
- (iv) taking $\mu_F \neq \mu_0$, to represent better the properties of sodium.

A more significant modification might be to replace the thin wall boundary conditions, derived here, with a wall of finite thickness h , with finite electrical conductivity (σ_W) and magnetic permeability (μ_W), as was done for a finitely conducting inner core in the geodynamo simulations of Glatzmaier and Roberts (1995,1996).

Acknowledgment. We thank the NSF for support under grants EAR-0652370 and EAR-0439922 and NASA for support via grants NNG06GD44G and NNX09AD89G. This research was begun in the Spring of 2008 during the Workshop on *Dynamo Theory* held at the Kavli Institute for Theoretical Physics at UC Santa Barbara, supported in part by the National Science Foundation under Grant No. PHY05-51164. We are grateful to Jean-François Pinton and to two referees for helpful comments on an earlier version of this paper. Jean-François suggested the possible usefulness of the decay rates computed in section 4.

References

- Bullard, E.C. and Gubbins, D., Generation of magnetic fields by fluid motions of global scale, *Geophys. & Astrophys. Fluid Dynam.*, 1977, **8**, 41–56.
- Gailitis, A., Lielausis, O., Platācis, E., Dementev, S., Ciferons, G., Gerbeth G., Gundrum, T., Stefani, F., Christen, M. and Will, G., Magnetic field saturation in the Riga dynamo experiment, *Phys. Rev. Lett.*, 2001, **86**, 3024–3027.
- Garaud, P. and Guervilly, C., The rotation rate of the solar radiative zone, *Astrophys. J.*, 2008, **695**, 799–808.
- Gissinger, C., Iskakov, A., Fauve, S. and Dormy, E., Effect of magnetic boundary conditions on the dynamo threshold of von Karman swirling flows, *Europhys. Lett.*, 2008a, **82**, 29001-1-5.
- Gissinger, C., Dormy, E. and Fauve, S., Bypassing Cowling’s theorem in axisymmetric fluid dynamos, *Phys. Rev. Lett.*, 2008b, **101**, 144502-1-4.
- Glatzmaier, G. A., Numerical simulations of stellar convective dynamos I. The model and method, *J. Comp. Phys.*, 1984, **55**, 461-484.
- Glatzmaier, G. A. and Clune, T. L., Computational aspects of geodynamo simulations, *Comp. Sci. Eng.*, 2000, **2**, 61-67.
- Glatzmaier, G. A. and Roberts, P. H., A three-dimensional convective dynamo solution with rotating and finitely conducting inner core and mantle. *Phys. Earth Planet. Int.*, 1995, **91**, 63-75.
- Glatzmaier, G. A. and Roberts, P. H., An anelastic evolutionary geodynamo simulation driven by compositional and thermal convection. *Physica D*, 1996, **97**, 81-94.
- Kageyama, A., Sato, T., Watanabe, K., Horiuchi, R., Hayashi, T., Todo, Y., Watanabe, T.H. and Takamaru, H., Computer simulation of a magnetohydrodynamic dynamo II, *Phys. Plasmas*, 1995, **2**, 1421–1431.
- Kaiser, R. and Tilgner, A., Kinematic dynamos surrounded by a stationary conductor, *Phys. Rev. E*, 1999, **60**, 2949–2952.
- Lowes, F.J. and Wilkinson, I., Geomagnetic dynamos; an improved laboratory model, *Nature*, 1968, **219**, 717–718.
- Monchaux, R., Berhanu, M., Bourgoin, M., Moulin, M., Odier, Ph., Pinton, J.-F., Volk, R., Fauve, S., Mordant, N., Pétrélis, F., Chiffaudel, A., Deviaud, F., Dubrulle, B., Gasquet, C., Marié, L. and Ravelet, F., Generation of magnetic field by dynamo action in a turbulent flow of liquid sodium, *Phys. Rev. Lett.*, 2007, **98**, 044502.
- Müller, U.. & Bühler L, *Magneto-fluid-dynamics in Channels and Containers*, 2001, Springer: Berlin, Heidelberg.
- Ravelet, F., Chiffaudel, A. and Daviaud, F., Toward an experimental von Kármán dynamo: Numerical studies for an optimized design, *Phys. Fluids*, 2005, **17**, 117104.
- Schmitt, D. and Jault, D., Numerical study of a rotating fluid in a spheroidal container, *J. Comp. Phys.*, 2004, **197**, 671–685.
- Soward, A.M. and Dormy, E., Shear-layers in magnetohydrodynamic spherical Couette flow with conducting walls, *J. Fluid Mech.*, 2009, accepted.
- Spence E.J., Reuter, K. and Forest, C.B., A spherical plasma dynamo experiment, *Astrophys. J.*, 2009, **700**, 470–478.
- Stieglitz, R. and Müller, U., Experimental demonstration of a homogeneous two-scale dynamo, *Phys. Fluids*, 2001, **13**, 561–564.
- Wu, C.C. and Roberts, P.H., On a dynamo driven by topographic precession, *Geophys. & Astrophys. Fluid Dynam.*, to appear, 2009.

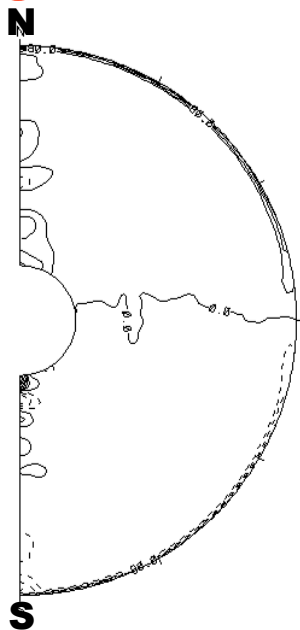
FIGURE CAPTIONS

Figure 1. A snapshot of the fluid flow structure for case 9. The bottom images are of the meridional (left) and radial (right) components; the top images are of the longitudinal component of the flow, the one on the left being translated into an angular velocity about the polar (NS) axis. The left-hand images are zonal averages in a meridian plane; the images on the right are structures on a spherical surface (an equal area projection) at a radius of 0.49m (i.e., just below the outer boundary). Reds and yellows represent positive values (i.e., outward or eastward) and blues represent negative values. The peak values in the upper left image are $\pm 40\text{m s}^{-1}$, which occur in a very thin boundary layer just below the outer boundary; the peak values in the upper right image are $\pm 20\text{m s}^{-1}$. In the lower left image the peak values are $\pm 2\text{m s}^{-1}$ and in the lower right they are $\pm 4\text{m s}^{-1}$.

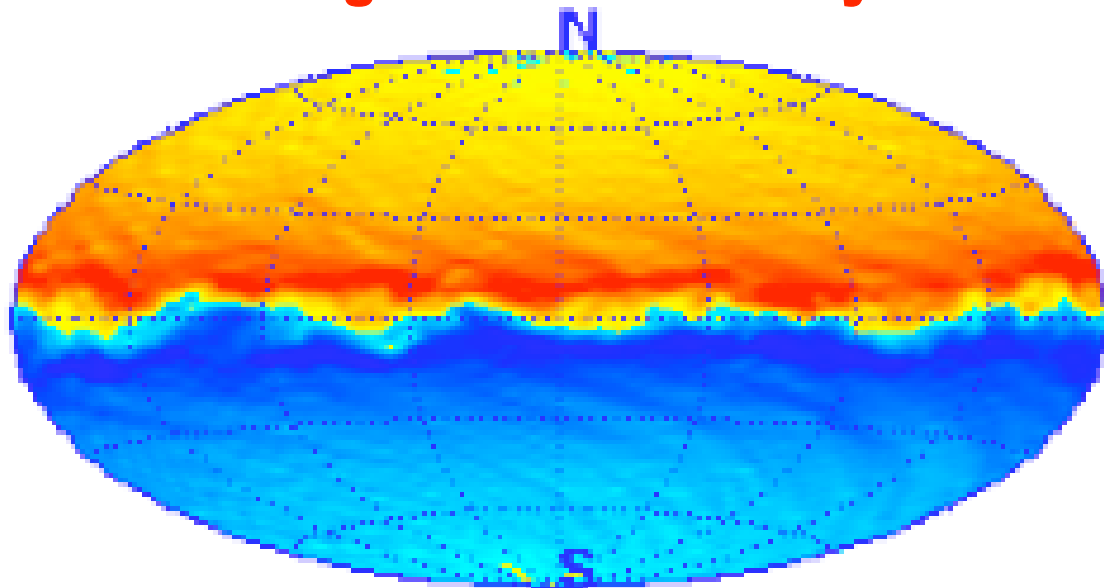
Figure 2. A snapshot of the field structure for case 9 (at the same time as that in figure 1). Similar views are displayed as those in figure 1, but here for the magnetic field instead of the fluid velocity. The peak intensity of the axisymmetric toroidal field in the top left image is 1100G, which occurs near the outer boundary at mid-latitude. The peak intensity in the top right image is 1200G. Reds and yellows in these two images represent eastward directed field of respectively greater and lesser strength. The solid lines in the bottom left image are axisymmetric poloidal magnetic field lines with a peak poloidal field intensity of $\pm 340\text{G}$. The radial field in the bottom right image peaks at $\pm 180\text{G}$ with reds and yellows representing outwardly directed field and blue inwardly directed field.

Figure 3. Evolution of the (logarithm of the) total magnetic energy, $M(t)$, within the fluid conductor V for (a) case 6, (b) case 9 and (c) case 10.

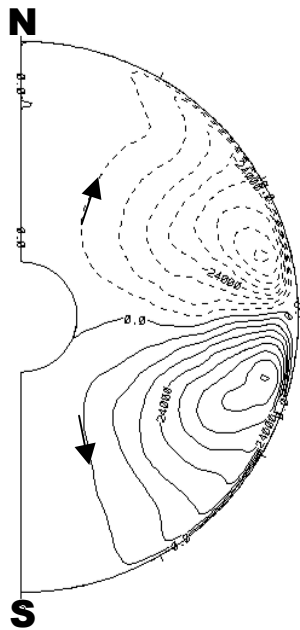
Angular velocity



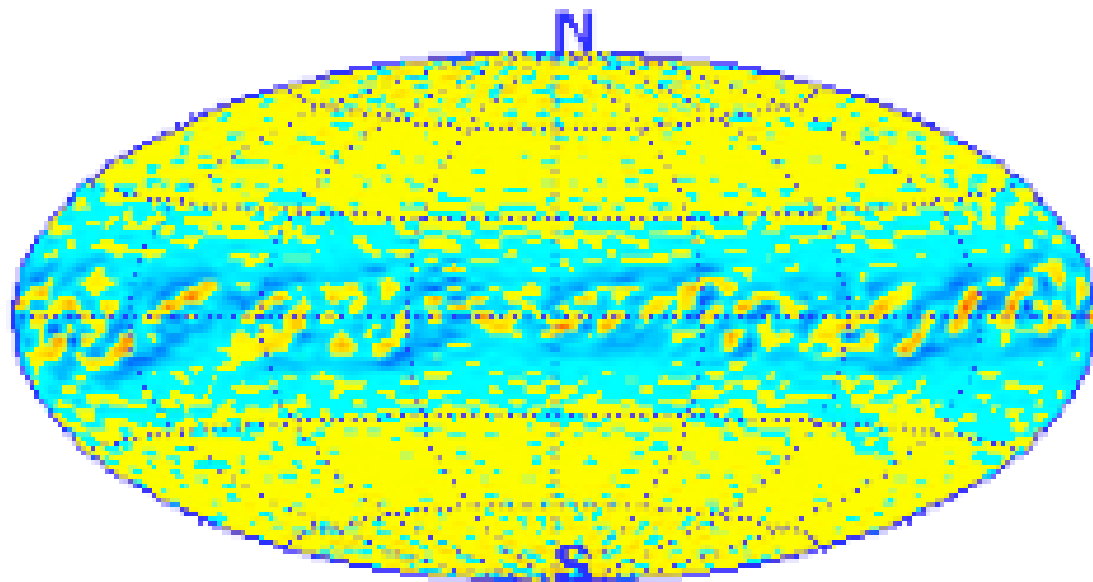
Longitudinal velocity



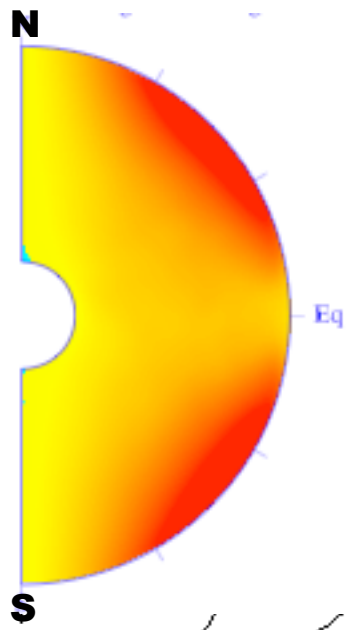
Meridional circulation



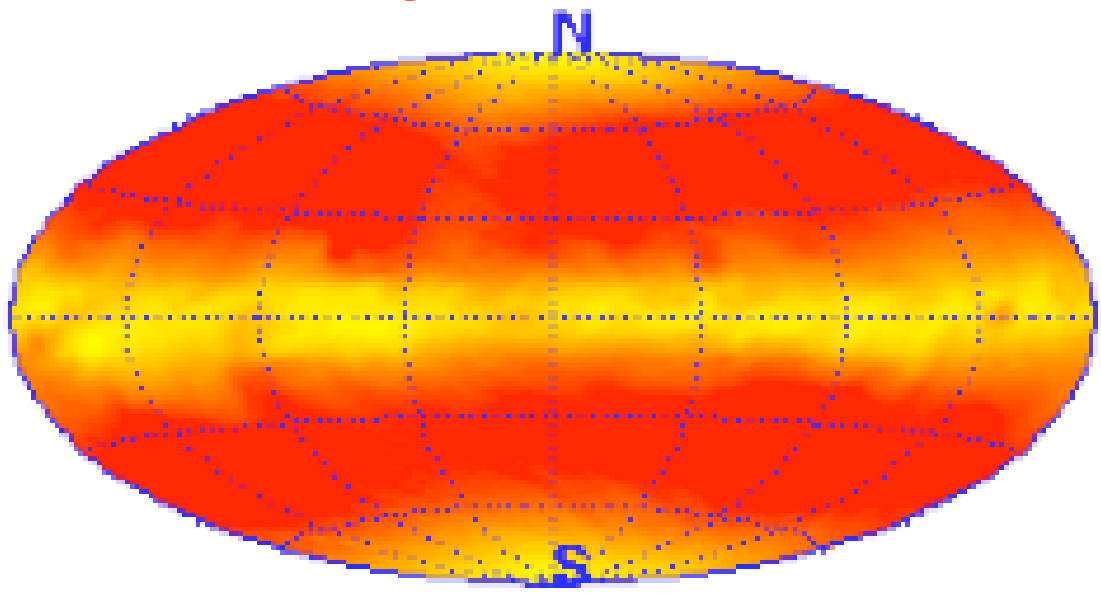
Radial velocity



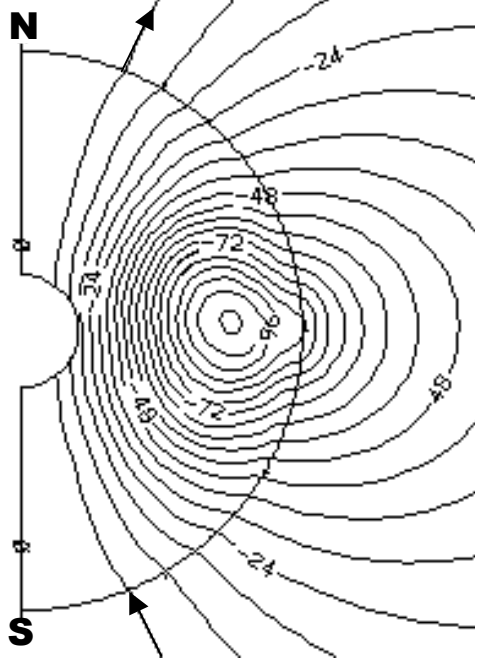
Toroidal field



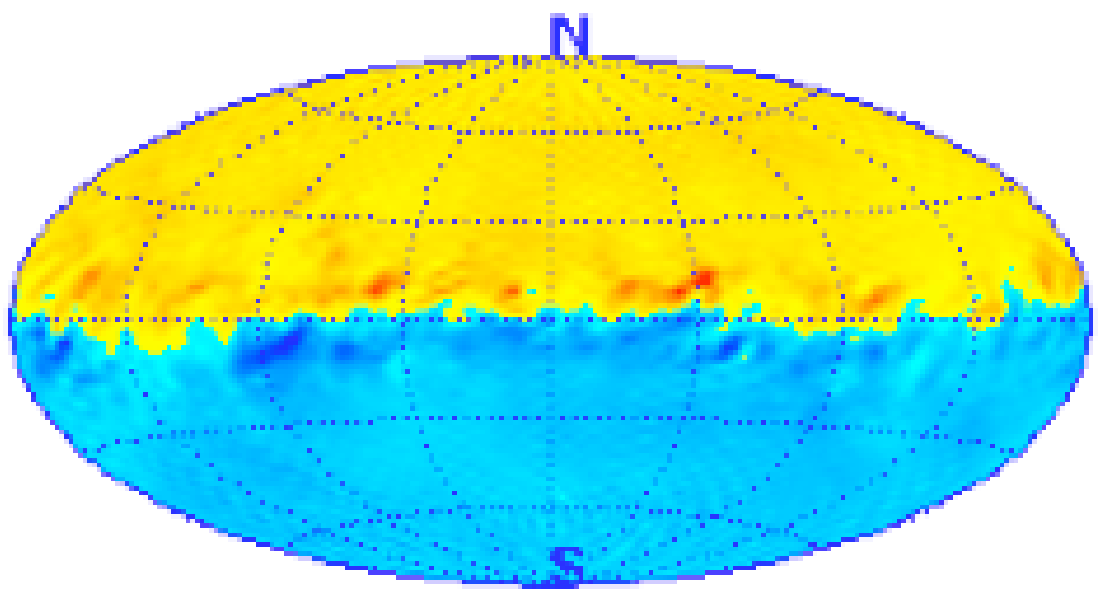
Longitudinal field



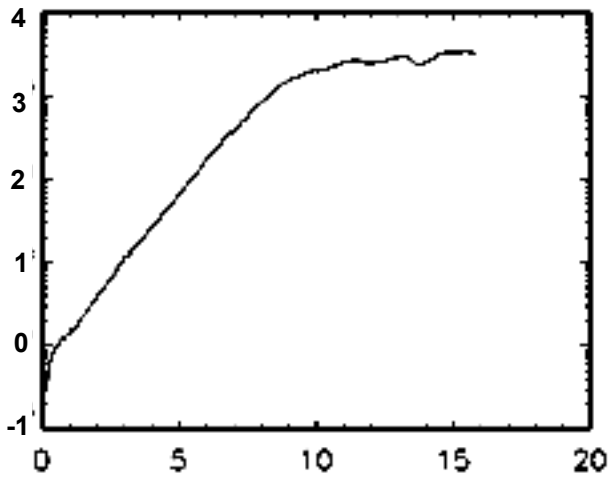
Poloidal field



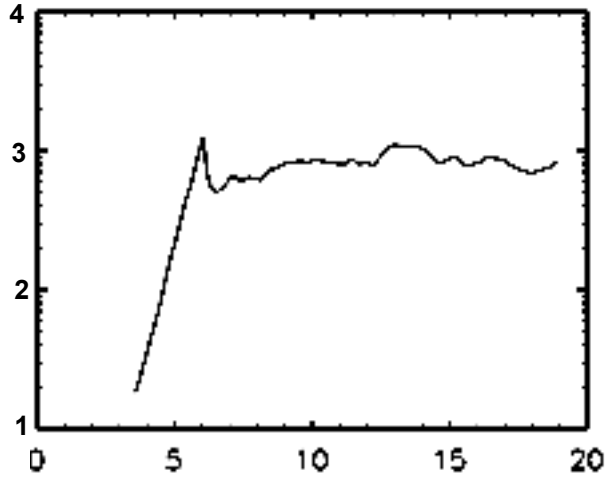
Radial field



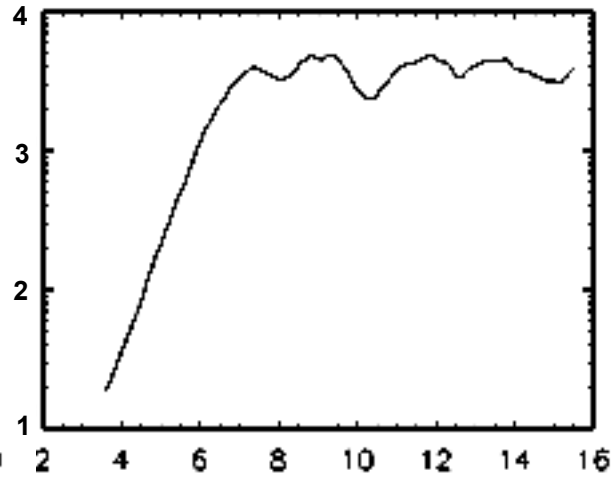
log magnetic energy (J)



seconds



seconds



seconds